



ARTICLE OPEN ACCESS

Imparting of Nearly Superparamagnetic Properties to Cryogel Scaffolds With Mesoporous MNPs for Magneto-Sensitive Tissue Engineering Strategies

Didem Demir¹  | Fatma Ulusal¹ | Hasan Ulusal² | Seda Ceylan³  | Sibel Dağlı⁴ | Nalan Özdemir⁵ | Mehmet Tarakçıoğlu^{2,6}

¹Department of Chemistry and Chemical Process Technologies, Vocational School of Technical Sciences at Mersin Tarsus Organized Industrial Zone, Tarsus University, Mersin, Turkey | ²Department of Medical Biochemistry, Faculty of Medicine, Gaziantep University, Gaziantep, Turkey | ³Department of Bioengineering, Faculty of Engineering, Adana Alparslan Türkeş Science and Technology University, Adana, Turkey | ⁴Department of Medical Microbiology, Faculty of Medicine, Hatay Mustafa Kemal University, Antakya, Turkey | ⁵Chemistry Department, Faculty of Science, Erciyes University, Kayseri, Turkey | ⁶Department of Medical Biochemistry, Medical School, Gaziantep Islamic Science and Technology University, Gaziantep, Turkey

Correspondence: Didem Demir (didemdemir@tarsus.edu.tr)

Received: 22 April 2024 | **Revised:** 1 August 2024 | **Accepted:** 1 August 2024

Funding: The authors received no specific funding for this work.

Keywords: chitosan | cryogel | gelatin | magnetic nanoparticle | scaffold | tissue engineering

ABSTRACT

This work reports the assembly of mesoporous iron oxide nanoparticles (meso-MNPs) with cryogel scaffolds composed of chitosan and gelatin. Meso-MNPs with a particle size ranging from 2 and 50 nm, a surface area of $140.52 \text{ m}^2 \text{ g}^{-1}$, and a pore volume of $0.27 \text{ cm}^3 \text{ g}^{-1}$ were synthesized on a porous SiO_2 template in the presence of PEG 6000 followed by leaching of SiO_2 . Different ratios of meso-MNPs were successfully incorporated into chitosan:gelatin cryogels up to an amount equivalent to the entire amount of polymer. The morphological structure and physicochemical properties of the cryogels were directly affected by the amount of MNPs. VSM curves showed that all composite cryogels could be magnetized by applying a magnetic field. In the context of the safety of magnetic cryogel scaffolds for use in biomedicine, it is important to note that all values are below the exposure limit for static magnetic fields, and according to cytotoxicity data, scaffolds containing meso-MNPs showed nontoxicity with cell viability ranging from 150% to 275%. In addition, microbial analysis with gram-negative and gram-positive bacteria showed that the scaffolds exhibited activity against these bacteria.

1 | Introduction

Thanks to the development of material design and new manufacturing processes, a large number of scaffolds with different morphology, geometry, and functional properties can be produced with the tissue engineering approach for use in the biomedical field. So far, natural and synthetic polymer-based scaffolds with various morphological structures such as porous, fibrous, hydrogel, micro-patterned, or spherical particles have been successfully designed using methods such as electrospinning [1], solvent casting [2], particulate leaching

[3], emulsion templating [4], gas foaming [5], freeze-thawing [6], and additive manufacturing [7]. In fact, studies on new-generation scaffolds with multilayered hybrid morphology by combining the techniques mentioned here continue to progress with high demand such as solvent casting–particulate leaching [3], electrospinning–three-dimensional (3D) printing [8], and electrospinning–freeze-thawing [9]. To create ideal scaffolds that can better remodel the native extracellular matrix (ECM) structure, biocompatibility, micropore size, high porosity, controllable biodegradability, and appropriate mechanical properties that will improve cell interactions are desired. In addition

This is an open access article under the terms of the [Creative Commons Attribution-NonCommercial-NoDerivs](https://creativecommons.org/licenses/by-nc-nd/4.0/) License, which permits use and distribution in any medium, provided the original work is properly cited, the use is non-commercial and no modifications or adaptations are made.

© 2024 The Author(s). *Biopolymers* published by Wiley Periodicals LLC.

to polymer combination, geometry, and internal structural cues, scaffolds that activate under external physical stimuli such as magnetic fields and magnetism are also of growing research interest.

In the last decade, magnetically responsive (magneto-responsive) scaffolds, as one kind of smart biomaterials, have been introduced into tissue engineering to achieve favorable outcomes in advanced drug delivery, cell guidance for tissue regeneration/formation, and in vivo monitoring of tissue engineering processes [10, 11]. Magneto-responsive scaffolds as drug carriers could revolutionize local drug delivery to patients to release drugs on-demand at specific concentrations through internal/external magnetic signaling [12]. On the other hand, magnetic field forces are converted into mechanical stimuli in cells and this orientation accelerates tissue regeneration. Studies on this phenomenon have also shown that paramagnetic scaffolds can promote bone, cartilage, vascular, nerve, and tendon tissue regeneration under magnetic fields and even play positive roles in regulating wound healing phenotypes for macrophages and fibroblasts [13]. After implantation of scaffolds, it is also necessary to monitor tissue structures over time to assess tissue development and functionality. For this field, magneto-responsive scaffolds allow in vivo imaging thanks to optimal tissue penetration and 3D spatial resolution [11].

The magneto-responsive scaffolds to be used for the abovementioned application areas can be created by combining a polymeric matrix with magnetic nanoparticles (MNPs). Previous reports have revealed that MNPs (<20–30 nm), such as ferrous ferric oxide (Fe_3O_4) particles, create superparamagnetic micro-environments that stimulate a large number of sensitive receptors on the cell surface and thus have the potential to enhance the process of tissue regeneration, especially in the treatments of bone diseases [14–17]. In addition, it has been reported that the mechanical properties of scaffolds are improved with the incorporation of Fe_3O_4 MNPs, which have high specific stiffness, specific strength, and large specific surface area, into the polymer matrix [16, 18].

Considering the advantages of Fe_3O_4 MNPs with the superparamagnetism properties they display, researchers have incorporated these MNPs into polymeric scaffolds for tissue engineering applications such as enhancing tissue regeneration [16, 19], targeted drug delivery [20, 21], and magnetic resonance imaging (MRI) [22]. In this study, we developed cryogel scaffolds composed of mesoporous iron oxide nanoparticles (meso-MNPs) that can be controlled by the applied magnetic field. The innovative aspect that distinguishes this research from the other studies lies in the synthesis strategy that imparts a mesoporous morphology to the nanoparticles. The porous Fe_3O_4 MNPs synthesized in the studies so far are generally in hybrid structures consisting of a Fe_3O_4 core and a mesoporous silicon dioxide (SiO_2) shell [23]. Herein, we first evaluated the interaction of meso-MNPs synthesized using polyethylene glycol (PEG 6000) molecules with chitosan cryogel scaffolds. In this way, the physicochemical properties of existing cryogels were preserved and the potential of meso-MNPs with magneto-responsive cryogel scaffolds for the field of tissue engineering was demonstrated.

2 | Materials and Methods

2.1 | Materials

For the construction of a 3D polymeric template as a scaffold, chitosan with medium molecular weight and gelatin for microbiology was selected and obtained from Sigma-Aldrich, USA. The other reagents for MNPs production, which are hydrochloric acid (HCl, 37%), tetraethyl orthosilicate (TEOS, 99%), PEG (with MW 6000 kDa), SiO_2 , and ethyl acetate (anhydrous, 99.8%), were also provided by Sigma-Aldrich, USA.

2.2 | Production of Meso-MNPs

Production of meso-MNPs consists of three steps as also described in our groups' previous recent studies including (i) the synthesis of mesoporous SiO_2 NPs, (ii) the coating of the synthesized SiO_2 NPs with Fe_3O_4 , and (iii) the subsequent leaching of SiO_2 after coating. The synthesis steps as detailed in recent previous studies by Ulusal et al. [24] and Ulusal and Özdemir [25] are schematically summarized in Figure 1 for a clear understanding. Briefly mentioned, in the first step, porous SiO_2 NPs were synthesized using PEG 6000 [26]. A solution of PEG at 3.2% concentration in 6% HCl was prepared. TEOS was added to the solution at 2.3 times the mass of PEG, and a white powdery product was obtained after 60 h at 80°C. The product was neutralized to pH 7.0 by washing with distilled water five times for 5 min at 10,000 rpm, dried in an oven, and burned at 550°C for 6 h. In the second step, to coat the mesoporous SiO_2 NPs with Fe_3O_4 ($\text{SiO}_2@ \text{Fe}_3\text{O}_4$ NPs), a dry synthesis method was applied using hexaurea iron (III) nitrate ($[\text{Fe}(\text{NH}_2\text{CONH}_2)_6](\text{NO}_3)_3$) complex as a precursor. A certain amount of complex was dissolved in triethylene glycol, and mesoporous SiO_2 prepared in the previous step was added to this mixture. The mixture was gradually brought to 260°C under magnetic stirring and kept in these conditions for 6 h. At the end of this period, the mixture was cooled to room temperature and washed in 100 mL of ethyl acetate by magnetic decantation until a transparent washing solution was formed. Finally, the synthesized $\text{SiO}_2@ \text{Fe}_3\text{O}_4$ NPs were washed with acetone and dried in an oven at 30°C. In the last step, for leaching silica, the known amount of dried mesoporous $\text{SiO}_2@ \text{Fe}_3\text{O}_4$ NPs was dispersed in 100 mL of distilled water with the help of an ultrasonic bath. Na_2CO_3 was added at a ratio of 1:5 by mass under stirring at 50°C for 24 h. The initially brown mixture turned dark brown at the end of this period. The obtained meso-MNPs were separated by decantation, washed with distilled water and acetone, and dried at room temperature.

2.3 | Production of Cryogel Scaffolds

The 3D cryogenic scaffold designed for the transport of meso-MNPs and as an artificial ECM was prepared in line with the optimization results obtained from our previous studies [27–29]. In this context, chitosan solution (3% wt.) was prepared in glacial acetic acid (2% vol.) at room temperature, and gelatin solution (6% wt.) was prepared in distilled water at 60°C. The homogeneously prepared polymer precipitates were mixed at a ratio of 1:1 by volume and crosslinked under cryogenic conditions by adding 3% vol. glutaraldehyde solution. After 24 h, the stabilized

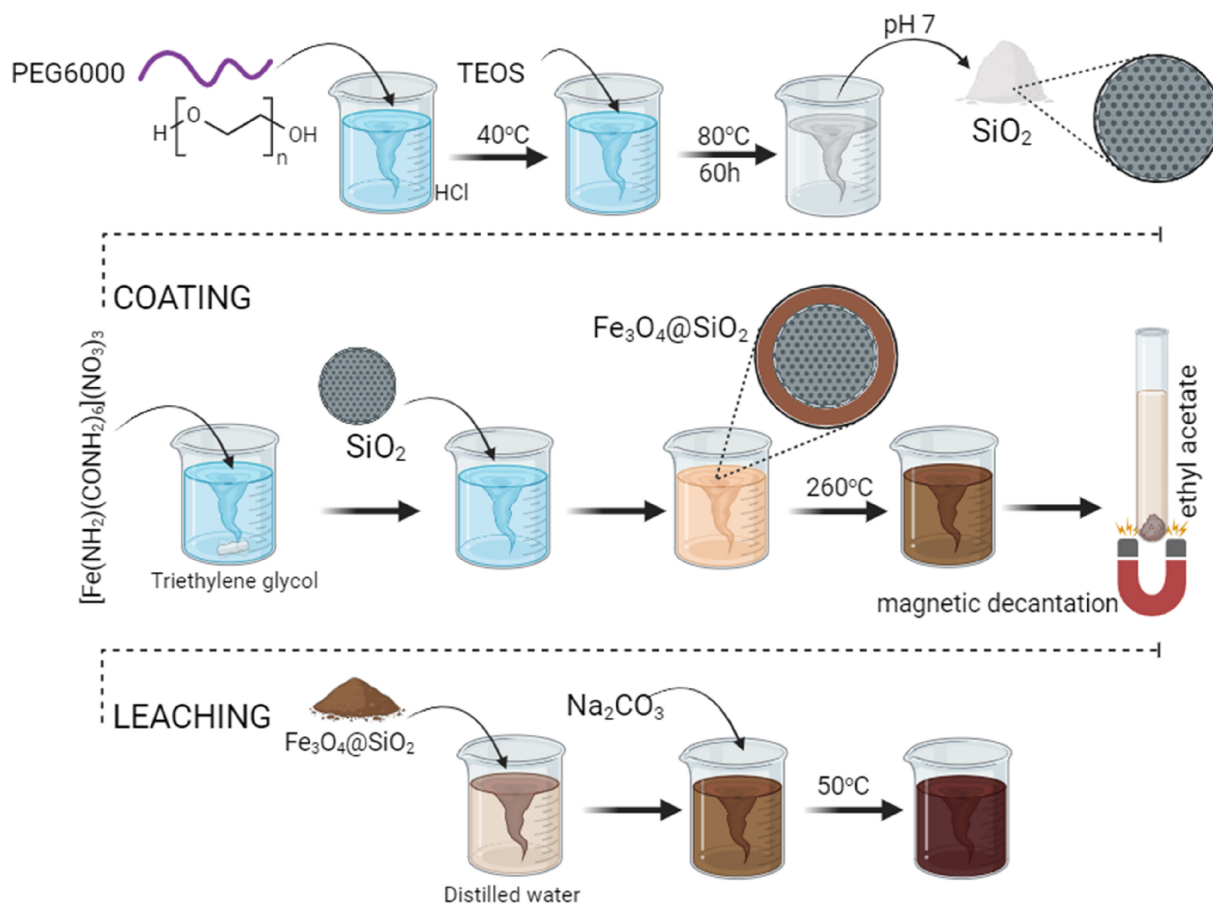


FIGURE 1 | Illustration of the production steps of mesoporous MNPs: (i) synthesis of mesoporous SiO_2 NPs, (ii) coating of the synthesized SiO_2 NPs with Fe_3O_4 ($\text{Fe}_3\text{O}_4@\text{SiO}_2$), and (iii) the subsequent leaching of SiO_2 to obtain mesoporous Fe_3O_4 NPs (meso-MNPs).

gels were brought to room temperature, washed with high volumes of distilled water, and subjected to lyophilization for drying without distorting their physical shape.

Meso-MNPs-added cryogel scaffolds were obtained by adding completely dried fine powder of meso-MNPs directly to the polymer solution and crosslinking the resulting composite solution in cryonic media under the abovementioned experimental conditions. For this purpose, based on the amount of polymer, meso-MNPs were added to the polymer mixture at 25, 50, and 100wt. % of the polymer. In the continuation of the study, depending on the increase in the amount of meso-MNPs, blank cryogels were named S0, and MNPs-loaded cryogels were named S25, S50, and S100, respectively.

2.4 | Characterization Studies of Meso-MNPs

For meso-MNPs characterization, magnetization measurements with a Vibrating Sample Magnetometer (VSM, Cryogenic Limited PPMS) were performed. The magnetization measurements were carried out by using VSM with a magnetic field range of up to ± 5 Tesla at room temperature. X-ray diffraction (XRD) patterns were recorded in the 2θ range of 10° – 90° with $\text{CuK}\alpha$ radiation ($\lambda = 0.154$ nm) using a Rigaku MiniFlex x-ray diffractometer. Morphological analyses were conducted using scanning electron microscopy (SEM, Zeiss Gemini 500) and transmission

electron microscopy (TEM, FEI Talos F200S) images. The operating accelerating voltages were 5 and 200 kV for SEM and TEM, respectively. The specific surface area was determined according to the BET method after N_2 adsorption–desorption.

2.5 | Characterization Studies of Cryogels

Synthesized cryogels were characterized by Fourier transform infrared spectroscopy (FTIR), SEM, pore size, swelling capacity, and magnetic properties. For chemical identification, FTIR spectroscopy (Perkin Elmer, 400 FTIR, USA) was performed ranging between 400 and 4000 cm^{-1} having 20 scans with a resolution of 4 cm^{-1} . For morphological investigations of the cryogels, SEM (Carl Zeiss, SUPRA 55, Germany) was used. After coating the freeze-dried cryogel samples with a thin layer of gold, the images were obtained at an accelerating voltage of 5 kV. The mean pore size was calculated by processing measurements of at least 50 pores in the SEM images taken using Image-J software. The swelling capacity of cryogels was determined from the difference in weights of the freeze-dried cryogel and swollen cryogel at predetermined time intervals (5, 15, 30, 60, 90, 120, and 150 min). First, the initial dry weight of cryogel samples was recorded (Wi). Samples were taken into a falcon tube containing 10 mL of phosphate-buffered solution (PBS pH 7.4) and the temperature was fixed to 37°C using a water bath. After each time, the samples were carefully taken and excess water around the

samples was removed using a filter paper. The swollen weight of samples was recorded (Wt). The swelling capacity of the cryogels, that is, the water content at each time interval, was calculated using the following equation:

$$\text{Swelling capacity, wt. \%} = [(Wt - Wi) / Wi] \times 100 \quad (1)$$

VSM (Cryogenic Limited PPMS) was used for determining the magnetic properties of cryogels after adding MNPs at different ratios. Before analysis, the samples were prepared by grounding the dried cryogels in a fine powder using a ceramic mortar. The powder samples were placed in a Teflon holder. The magnetic properties were then determined by an increasing magnetic field over the sample. The measurements were carried out at room temperature with a magnetic field range up to ± 5 Tesla.

2.6 | Cell Studies

The scaffolds were cut at a height of 3.0 mm and a radius of 2.5 mm and placed in 24-well plates for cell viability assays. The scaffolds were sterilized before analysis. For the sterilization, the samples were first soaked in 70% alcohol for 1 h. Then, the alcohol was removed and washed three times with sterile PBS (Cytiva, USA). After the last wash, 1 h was left for drying. Cells were observed during drying and care was taken not to dry completely. A549 and BEAS2B cells were counted. Cell suspensions of $40\text{--}50 \times 10^3$ cells in $20 \mu\text{L}$ were carefully added onto the scaffolds. The cell-free group from each scaffold (3D control) and the cell group without scaffold (2D control) were also added to the plates. The plates were kept in an incubator for 2 h at 95% humidity, 5% CO_2 , and 37°C for 2 h for the cells to adhere. After 2 h, DMEM medium (Cytiva, USA) containing 10% FBS and 1% penicillin was added to the scaffolds and incubated for 1 and 3 days in the incubator. At the end of the incubation periods, the cell media were removed and the CCK-8 (Abbkine, USA) viability test was performed. According to this test, $10 \mu\text{L}$ of CCK-8 reagent was added to the media and incubated at 37°C for 2.5 h, and at the end of the incubation, the absorbance was measured at 450 nm after shaking for 10 s. For scaffold-free cells (2D), viability was considered 100%. Cell-free scaffolds (3D) were considered blind and absorbance values were subtracted. All experimental groups were performed with two repetitions.

2.7 | Antibacterial Analysis

The agar well diffusion method was used to analyze the inhibitory effect of cryogel scaffolds against pathogenic microorganisms [30, 31]. Gram-positive *Staphylococcus aureus* (ATCC 29213) and gram-negative *Escherichia coli* (ATCC 25922) bacteria were inoculated on 5% sheep blood agar plates and incubated at 37°C for 24 h. After incubation, a homogeneous bacterial density of 0.5 McFarland standard (1.5×10^8 CFU mL) was prepared with sterile distilled water from the prepared pure bacterial colonies. For the agar well diffusion method, Muller-Hinton agar (MHA) was sterilized in an autoclave at 121°C for 15 min, then poured onto sterile plates at a height of 4 mm and allowed to dry for 15 min. After inoculation on the MHA plate, $100 \mu\text{L}$ of the bacterial suspension prepared according to the McFarland standard with a density of 0.5 was spread with sterile swabs. After

15 min of drying in a sterile cabinet, wells with a diameter of 8 mm were formed on the plate surface with the help of a sterile cork borer. Then, $192 \mu\text{L}$ of sample was inoculated into each of the wells created based on the volume calculation [32]. After incubation of the plates at 37°C for 24 h, the inhibition zone diameter of each well was measured. The experiments were performed in a laminar flow sterile cabinet and repeated three times.

3 | Results and Discussion

3.1 | Characterization Studies of MNPs

The synthesized meso-MNPs were morphologically characterized using SEM and TEM images presented in Figure 2A,B, respectively. In general, the morphology of the novel particles was found to be quite similar to each other, exhibiting uniform spherical or almost spherical structure with particle sizes in the nano range. It is seen that the surface of the particles exhibits porous bumpy-like structures. A similar morphological identification was reported in another study where iron oxide mesoporous magnetic microparticles were produced by El-Boubbou et al. [33]. Although the “mesoporous” term was defined, it was very difficult to observe the porous structure of nanoscale particles in morphological images. Therefore, BET analysis was performed to reveal the surface area of the synthesized particles due to their porous structure. According to the BET analysis (Figure 2C), the pore diameters of MNPs ranged between 2 and 50 nm, and the average pore diameter was calculated as 4.43 nm, confirming the Type IV isotherm. It was also determined that the surface area of meso-MNPs was $140.52 \text{ m}^2 \text{ g}^{-1}$ and the pore volume was $0.27 \text{ cm}^3 \text{ g}^{-1}$. Moreover, the XRD pattern of the meso-MNPs was characterized as shown in Figure 2D. All the diffraction peaks present in the XRD pattern correspond to the single-phase Fe_3O_4 (magnetite) cubic crystals (JCPDS 19-0629) in correlation with other studies [24, 34].

After determining the morphological observations of meso-MNPs, the magnetic properties were characterized using magnetic hysteresis loops and the behavior of meso-MNPs under an external magnetic field. In Figure 3A, the behavior of MNPs dispersed in water under the external magnetic field created by the magnet is photographed depending on time. Initially, it can be seen that MNPs were successfully dispersed in distilled water without coagulation and displayed a homogeneous appearance. It was observed that in the first 60 s, it started to rapidly gather around the magnetic field, and at the end of approximately 5 min, the solid MNPs were completely separated from the liquid phase. The magnetic characterization of meso-MNPs was continued with VSM analysis, which is used to measure the magnetic moment of a sample when it vibrates perpendicular to a uniform magnetizing field. Magnetic field dependence of magnetization (M - H) measurement was performed by sweeping the magnetic field in the range of $\pm 1 \text{ T}$ at room temperature. Figure 3B shows the hysteresis loop of meso-MNPs. It can be seen in Figure 3B that synthesized meso-MNPs show hysteresis characteristic with a very low coercive field (Hc-16 Oe) at room temperature. In addition, magnetization is not saturated up to 1 T for meso-MNPs. Saturation magnetization of sample was determined as 21.30 emu g^{-1} . Considering M_s , Hc, and particle size (23.86 nm on average) of meso-MNPs, it can be suggested that the sample shows ferrimagnetic characteristics. This

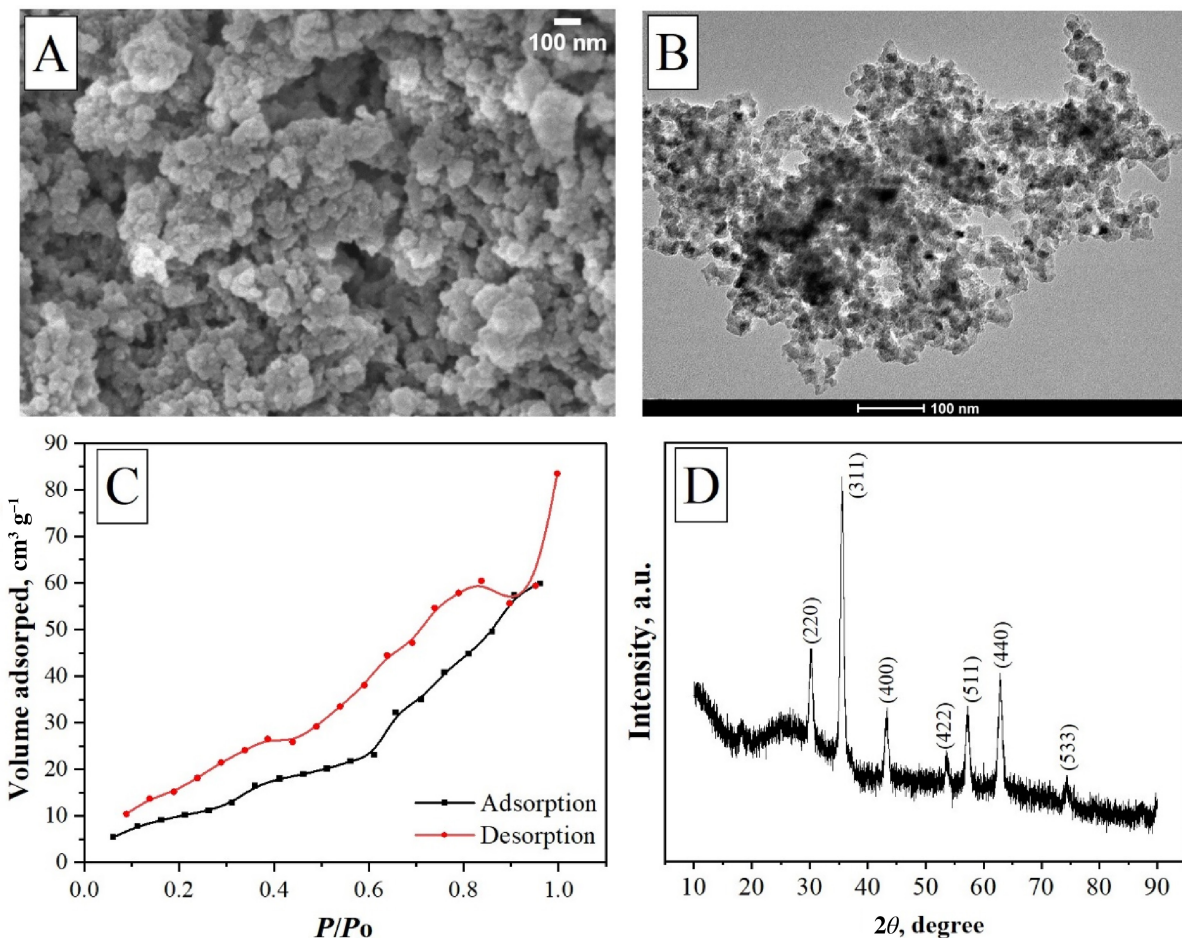


FIGURE 2 | Characterization of meso-MNPs: (A) SEM image at 100 nm scale bar, (B) TEM image at 100 nm scale bar, (C) BET analysis, and (D) XRD analysis.

is because that the particle size is smaller than critical phase transition size of Fe_3O_4 (25 nm). Ms value of sample is lower than of the bulk Fe_3O_4 (90 emu g^{-1}). This structural behavior can create a noncollinear spin arrangement in structure and decrease saturation magnetization of meso-MNPs [34–36].

3.2 | Characterization Studies of Cryogels

The second part of the study aimed to activate the scaffolds under a magnetic field by incorporating novel superparamagnetic meso-MNPs into the chitosan:gelatin cryogel structure. In this context, three different ratios of MNPs (25, 50, and 100 wt. %) were directly incorporated into the polymer solution, and by freezing the composite solution in cryogenic conditions in the presence of cross-linker, meso-MNPs-loaded cryogel scaffolds were successfully obtained. Figure 4A shows the photographs of the neat (S0) and meso-MNPs-loaded cryogels (S25, S50, and S100) after freeze-drying. Gels produced in plastic syringes were obtained in cylindrical form and stable without any deformation. It can be seen that as the MNPs ratio increases, the color of the gels goes from light to dark. In fact, the S100 cryogel showed a color close to dark brown compared to the others. Also in other studies, the color intensity has been correlated with the amount of MNPs in polymer structures [20, 37, 38]. This is due to the natural color of Fe_3O_4 , and this color change is an indication that MNPs can be physically integrated into the cryogel.

VSM analysis was performed to measure whether meso-MNPs imparted magnetic properties to the cryogels. As expected, it was found that there was an increase in magnetic properties along with an increase in MNP concentration. VSM curves showed that all-composite cryogels could be magnetized by applying a magnetic field. The saturation magnetization was 21.30 emu g^{-1} for the synthesized meso-MNPs (Figure 2B), 0.86 emu g^{-1} (S25), 1.29 emu g^{-1} (S50), and 2.36 emu g^{-1} (S100) for the cryogels, respectively. The significant decrease in saturated magnetization can be attributed to the trapping of meso-MNPs within the pore walls in the cryogels. In a study by Jia et al. [18], the saturated magnetization value of chitosan: Fe_3O_4 composite NPs prepared using Fe_3O_4 with a saturated magnetization of 120 emu g^{-1} was approximately 11.15 emu g^{-1} . Similarly, in this study, the magnetization value of Fe_3O_4 nanoparticles coated with chitosan polymer decreased significantly [39]. After doping MNPs into cryogels, the samples showed small magnetization. We can explain the reason for this as follows: when meso-MNPs were added to the chitosan:gelatin cryogel structure, Fe_3O_4 increased the magnetic interaction and the material began to show magnetic properties, albeit weakly, especially at low MNPs amounts (S25 and S50). Although it can be seen here that the magnetic interaction of cryogels can be increased due to the increase in the amount of MNPs, it can be said that the superparamagnetic property of meso-MNPs decreases and exhibits nearly superparamagnetic properties in the cryogel samples formed with the MNPs amounts used in the study.

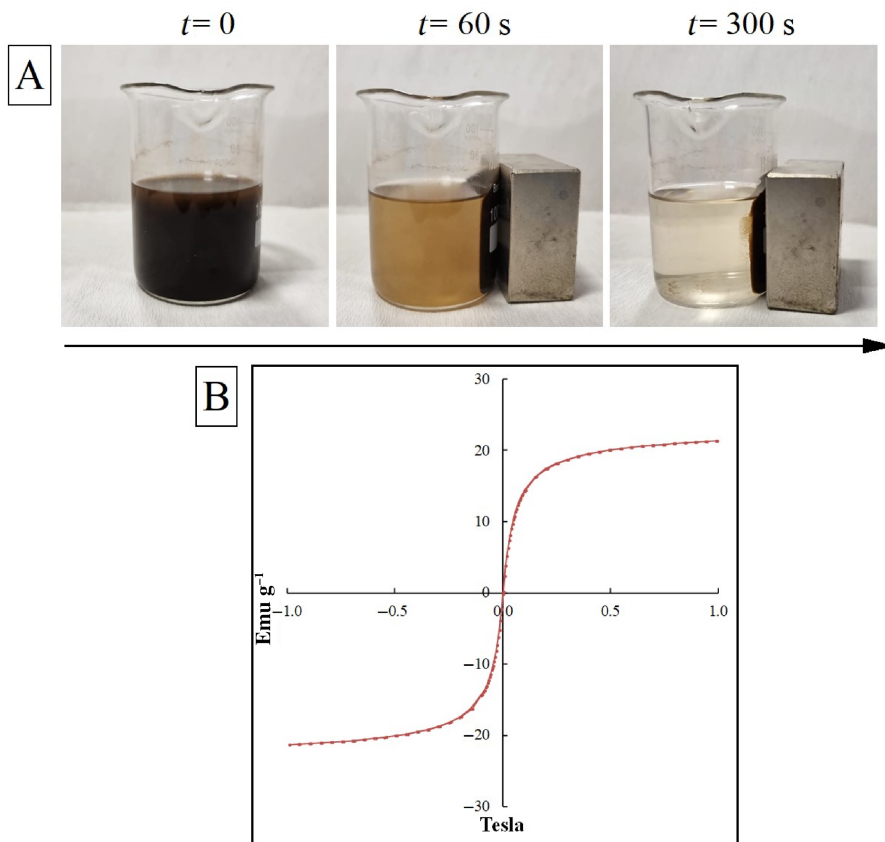


FIGURE 3 | Characterization of MNPs: (A) time-lapse photos of the capture of MNPs in diluted suspension with an external magnet and (B) VSM magnetic hysteresis curves showing the magnetic properties of meso-MNPs.

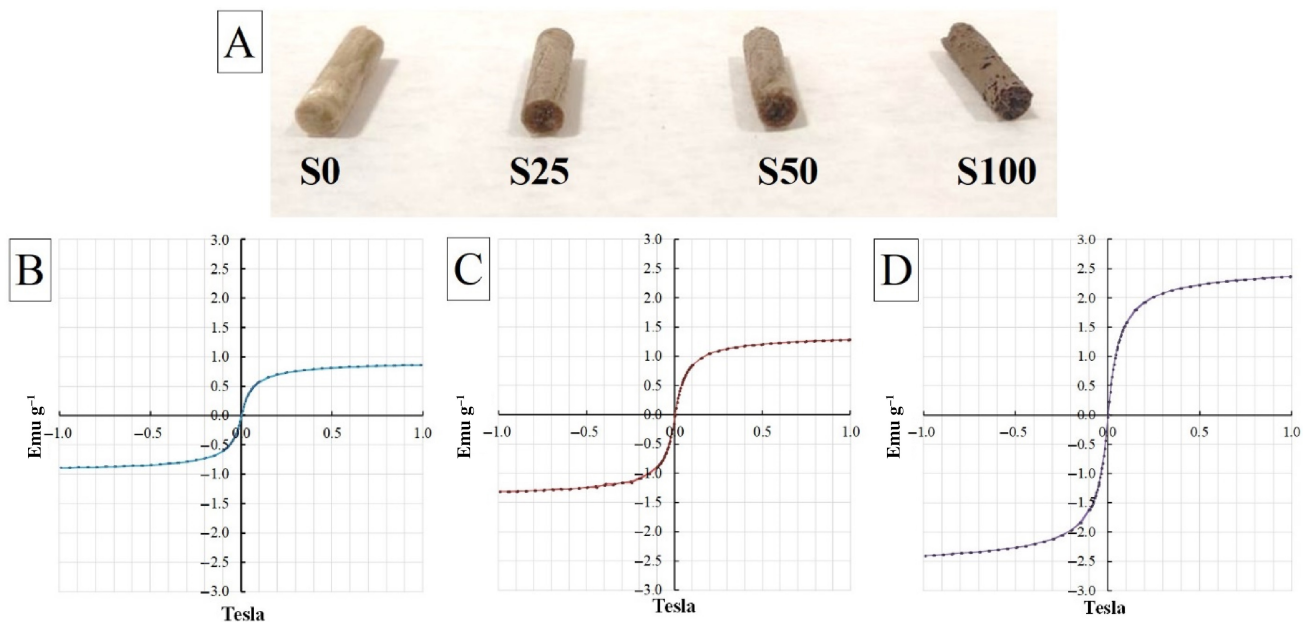


FIGURE 4 | (A) Photos of scaffolds without and with the presence of an increased amount of porous MNPs and VSM curve graphs of (B) S25, (C) S50, and (D) S100 ferromagnetic cryogel scaffolds.

In the evaluation of magnetic cryogel scaffolds in terms of safe use in biomedicine, all values are below the static magnetic field (SMF) exposure limit of 400 mT published in the International Commission on Non-Ionizing Radiation Protection SMF exposure guidelines [40]. Therefore, we can conclude that the

meso-MNPs-loaded magnetic scaffolds prepared in this study can be safe for human body use as reported by Shao et al. [41].

Regarding the potential use of cryogel scaffolds in tissue engineering applications after different amounts of meso-MNPs

incorporation, the changes in the characteristics of scaffolds were evaluated by a series of physicochemical analyses. In terms of scaffold morphology for a successful tissue engineering application, it has been demonstrated that microarchitecture has a major impact on cell behaviors in both in vitro and in vivo settings. Specifically, the scaffold's mean pore size can

efficiently modify the cell-matrix interaction. Larger scaffold holes have been shown to promote cell migration and diffusion, while smaller ones increase the scaffold's surface area for cell attachment. The biochemical and mechanical characteristics of regenerated constructions may be influenced by the ensuing cell proliferation, differentiation, and matrix deposition.

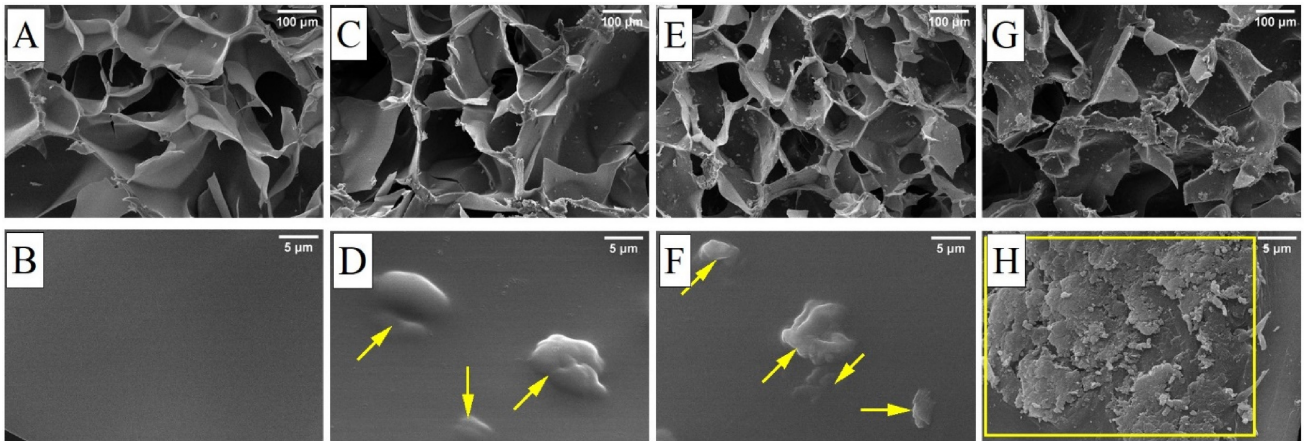


FIGURE 5 | Morphological evaluation of cryogel samples with SEM images taken at 100 \times and 10,000 \times magnifications: (A, B) S0, (C, D) S25, (E, F) S50, and (G, H) S100. (Areas marked in yellow indicate the collection points of particles on polymer walls inside the pores.)

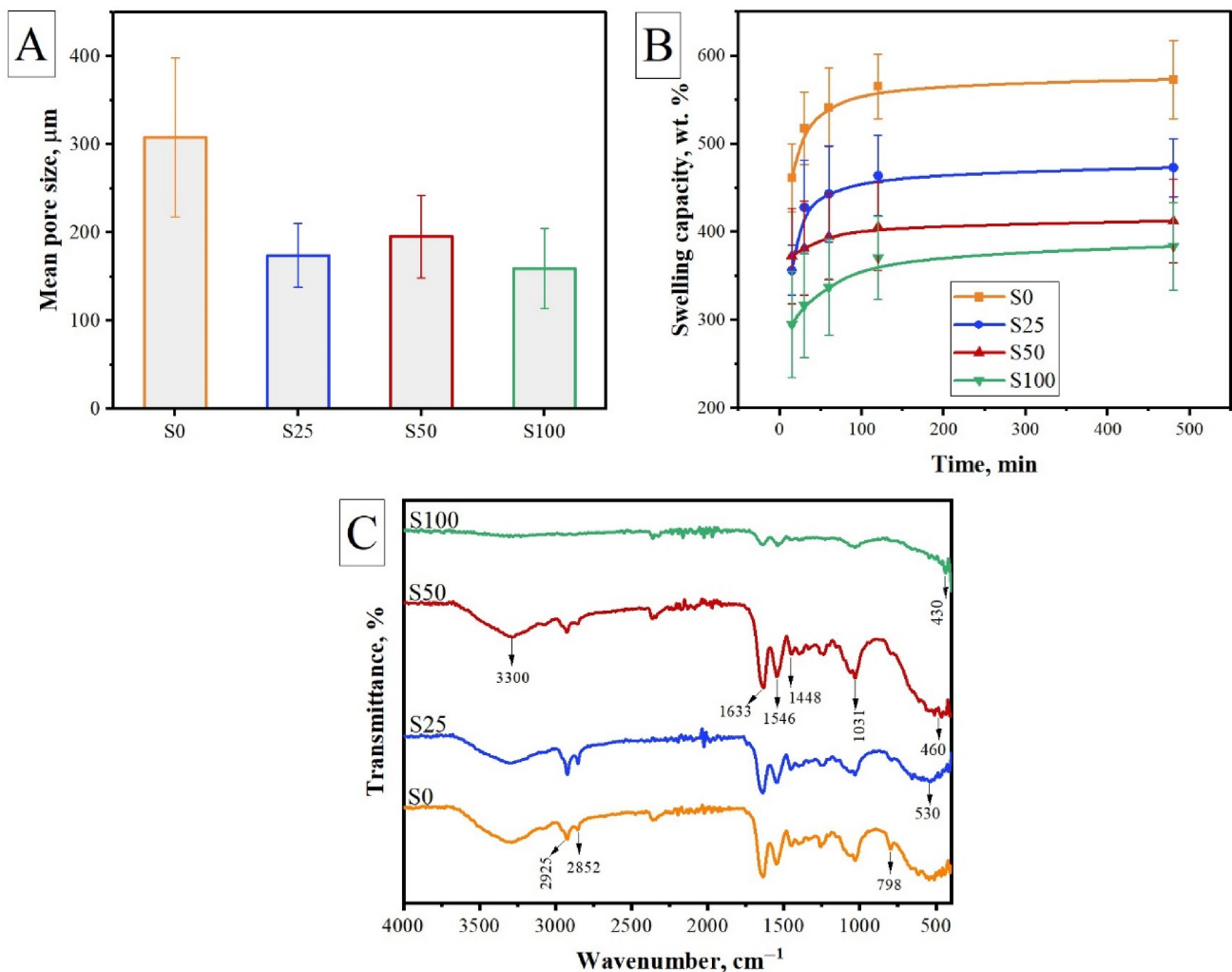


FIGURE 6 | Characteristics of cryogels: (A) mean pore size, (B) swelling capacity, and (C) chemical structure.

Consequently, different scientific groups study to understand which scaffold design (e.g., mean pore size) influences cell behavior and subsequent tissue creation [42].

In our research, an open and interconnected pore morphology was expected in all samples as a result of cryotropic gelation as the chosen manufacturing process. The morphological study by SEM (Figure 5) confirmed this expectation and revealed a highly porous structure for all cryogels. With the incorporation of meso-MNPs at different ratios, a porous structure with particles inside the pore was observed (Figure 5C,E,G). It is difficult to say that there is a significant change in porosity in the overall SEM images with increasing amount of MNPs. Therefore, when the SEM images obtained at higher magnifications were examined (Figure 5D,F,H), the presence of nanoparticles was found to be located on the polymer walls inside the pores (the collection points of particles are indicated by yellow markings). The presence of nanoparticle aggregation was observed especially in the S100 sample where the amount of meso-MNPs was the highest. Here, it can be said that a more homogeneous non-coagulated distribution occurred in samples S25 and S50 samples.

In addition to displaying the porous structure, determining the mean pore size is an essential criterion for determining which application the scaffold is more suitable for [43]. Studies in the literature have reported that scaffolds with an average pore diameter between 5 and 15 μm are more suitable for fibroblast ingrowth, 20–125 μm for adult mammalian skin, 100–200 μm for osteoblast regeneration, and 40–100 μm for osteoid ingrowth [44–46]. For this reason, the average pore diameter of each scaffold was calculated by processing SEM images with

Image-J. According to Figure 6A, the mean pore size was calculated as 307.71 ± 90.36 , 174.15 ± 36.26 , 195.46 ± 46.88 , and $159.47 \pm 45.51 \mu\text{m}$ for S0, S25, S50, and S100 cryogels, respectively. It can be said that the average pore size decreased with the addition of MNPs and settling in the polymer network. In parallel with these results, when the swelling values presented in Figure 6B are examined, it is seen that the swelling capacity of cryogels is related to the pore size. As the MNPs fill into the pore, it may be difficult for water to penetrate the gel structure. However, the swelling values obtained are still quite high due to the cryogenic structure of the scaffolds. The pore size and total porosity of the swollen samples increase, which maximizes the internal surface area of the scaffolds. Samples that exhibit a higher degree of swelling will have a larger surface area to volume ratio, allowing for maximum cell infusion into the 3D scaffold and optimal cell growth through better attachment to the scaffold surface [47].

The addition of different amounts of meso-MNPs resulted in some changes in the final morphological and physical properties of the cryogel scaffolds as discussed above. These changes were directly dependent on the amount of MNPs. Therefore, it is important to determine whether this interaction between MNPs and polymers is physical or chemical. For this reason, FTIR spectra of the cryogels were obtained as presented in Figure 6C. The characteristic peaks of the imine C=N group formed by the crosslinking reactions between amino groups of chitosan and gelatin with aldehyde groups of glutaraldehyde were observed at 1546 and 1633 cm^{-1} [48]. Overlapping peaks of O–H and N–H stretching were recorded at approximately 3300 cm^{-1} . The peaks observed at 2925 and 2852 cm^{-1} correspond to aliphatic

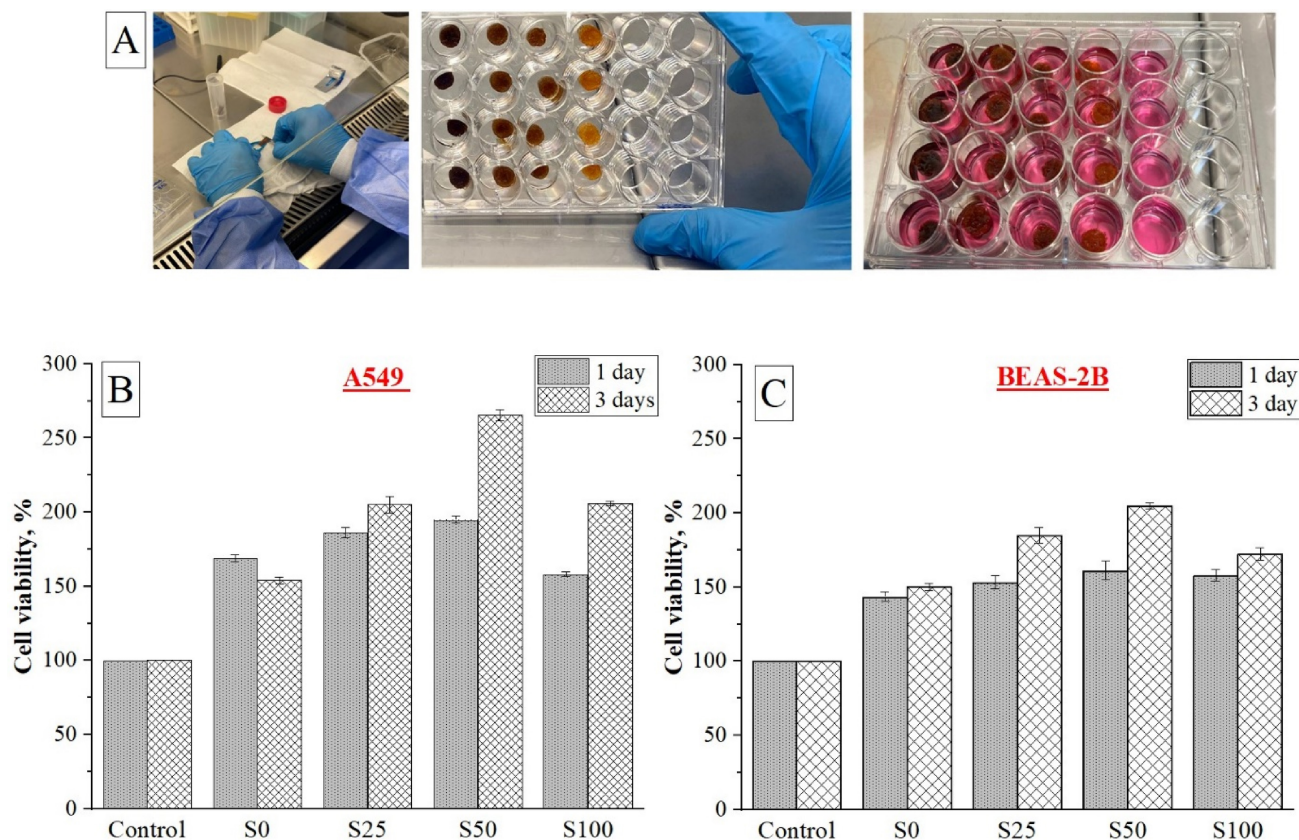


FIGURE 7 | Cell viability of A549 and BEAS-2B cells seeded on cryogel scaffolds and cultured for up to 3 days, assessed via CCK-8 assay.

C-H symmetric and asymmetric bonds, respectively [47, 49]. With the addition of meso-MNPs, the spectrum showed similar bands. However, especially, in the spectrum of S50 and S100, the peak of Fe–O vibration at 530 cm^{-1} shifted to 460 and 430 cm^{-1} due to the interaction between meso-MNPs and chitosan as also reported in another study [50]. In another study, Qiang et al. [51] stated that the hydrogen and amino groups of chitosan can form strong interactions with Fe_3O_4 surfaces. According to these, the results imply that meso-MNPs are successfully incorporated into the polymer network by hydrogen bonds formed between amino groups of chitosan and the oxygen atoms on Fe_3O_4 .

3.3 | Cytocompatibility of Scaffolds With Increased Amount of Meso-MNPs

The safety of the use of MNPs has not yet been clearly established. These particles tend to degrade in the body, therefore, in addition to the toxicity of the particles as a whole, the biocompatibility of the degradation products interacting in the body should be well understood [52]. Our primary goal in this study was to provide superparamagnetic properties to existing cryogel scaffolds without changing their morphological and physical properties. In this context, as stated in previous sections, the scaffolds preserved their characteristic properties with the addition of MNPs and gained nearly superparamagnetic properties

that will play an active role under magnetic field. Within the scope of these preliminary evaluation studies, in vitro cytotoxicity studies of cryogels produced with different amounts of MNPs (S25, S50, and S100) were also conducted and compared with the control sample (S0). Although these results do not provide direct information about the dose and time-dependent degradation products of meso-MNPs, they are important in terms of preliminary cytotoxicity evaluation. Figure 7 shows the CCK-8 test findings for A549 and BEAS-2B cells shown in cryogel scaffolds after 1 and 3 days in culture. According to the cytotoxicity data, the scaffolds containing meso-MNPs were nontoxic and cell viability ranged from 150% to 275%. These values indicating that the scaffolds were biocompatible for both cell types. When cell types were compared within themselves, it was observed that the A549 cell line exhibited a higher rate of cell viability than BEAS-2B. This shows that MNPs-loaded cryogel scaffolds have the potential to be evaluated to create an in vitro tumor model for this cancer cell line.

In different research articles, Fe_3O_4 has been used with different polymers such as [53, 54], PCL [55–57], PLLA, and gelatin [58] for various applications. In a study conducted by Panseri et al. [59], magnetic scaffolds were formed based on collagen and hydroxyapatite/collagen, and it was reported that the attraction of cells and growth factors was due to the presence of magnetic particles [59]. Similarly, in our study, it was observed that

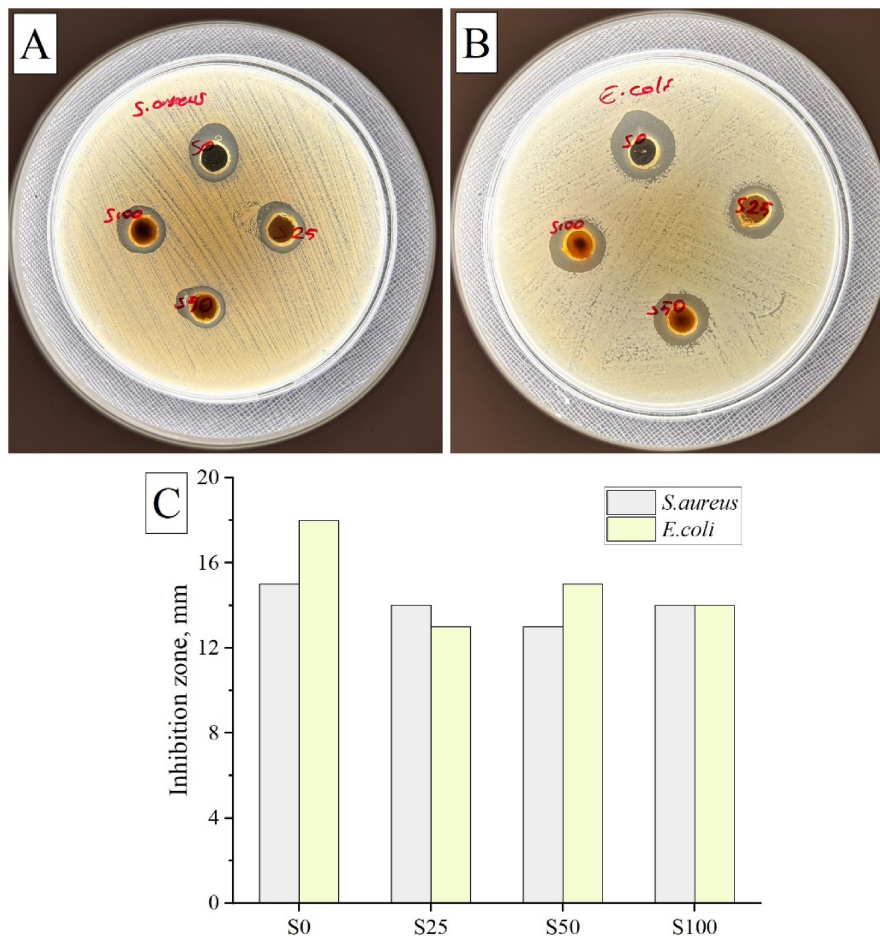


FIGURE 8 | Antibacterial activity of cryogel scaffolds. Agar well photographs of scaffolds against (A) *Staphylococcus aureus* and (B) *Escherichia coli* bacterial strains. (C) Inhibition zones obtained from the test results.

MNPs-loaded S25 and S50 scaffolds exhibit higher cell viability than S0 sample.

3.4 | Microbial Evaluation of Cryogel Scaffolds

Implantation-induced microbial infections can significantly affect cell survival and increase the risk of implant failure. Therefore, the production of scaffolds with antimicrobial materials is crucial for the success of scaffolds. In this study, chitosan, one of the selected polymers, is known to be antibacterial in nature [60–62]. In this part of our study, we determined the antibacterial activity of the scaffolds against gram-negative and gram-positive bacterial strains to see whether the antibacterial properties of the scaffolds were maintained after the addition of meso-MNPs. Figure 8 shows the agar well diffusion results of S0, S25, S50, and S100 cryogels against *S. aureus* and *E. coli*. It was observed that all samples formed an inhibition zone against both bacterial species.

4 | Conclusions

Combining therapeutic strategies in tissue engineering has proven to be a critical step in improving outcomes. Based on this, in this study, we functionalized chitosan:gelatin cryogel scaffolds with MNPs additive and developed composite scaffolds with potential for use in magneto-responsive tissue engineering applications. The synthesis of mesoporous MNPs was successfully carried out and the average particle size obtained was determined to be 4.43 nm. The synthesized meso-MNPs were used together with chitosan:gelatin cryogel and composite scaffolds with an open pore structure and interconnected porosity were successfully produced at different MNPs ratios. The incorporation of meso-MNPs into the gel matrix resulted in cryogel scaffolds with tailored morphological, physicochemical, and biological properties which are required for tissue engineering applications. SEM images confirmed that MNPs were successfully incorporated into the matrix without compromising significantly the inherent porous nature of cryogels. Depending on the amount of MNPs, accumulation of MNPs in the polymer wall or the pores was encountered. Although a shrinkage of the pores of the gels occurred due to this accumulation, no significant changes in swelling properties were recorded. In terms of biological studies, cytotoxicity, and antibacterial studies were performed. As a direct consequence of the interaction between MNPs and cells, we demonstrated that MNPs-added composite scaffolds have better cell viability after 3 days of incubation. The composite scaffolds were also found effective against bacterial strains such as *S. aureus* and *E. coli* in the presence of meso-MNPs. According to all results, we think that the composite cryogels produced in our study are an innovative tissue engineering product. Here, the use of meso-MNPs for tissue engineering applications is reported together with cryogel scaffolds. The incorporation of meso-MNPs into the polymeric network structure resulted in the acquisition of nearly superparamagnetic properties by the composite cryogels without a notable alteration in the conventional cryogel structure. The preliminary optimization results obtained from this study indicate that the meso-MNP-loaded cryogels have the potential to be employed in magneto-sensitive applications, including magnetically

stimulated drug delivery, stimulation of cellular responses under external magnetic fields, and targeting approaches for cancer therapy.

Author Contributions

Didem Demir: investigation, methodology, chemical and analytical research, data curation, and writing – original draft. **Fatma Ulusal:** methodology and analysis of meso-MNPs. **Hasan Ulusal:** methodology and analysis of in vitro biological studies. **Seda Ceylan:** analysis of scaffolds, writing – original draft. **Sibel Dağlı:** methodology and analysis of antibacterial studies. **Nalan Özdemir:** supervision, editing. **Mehmet Tarakçoğlu:** supervision, editing. All authors have read and agreed to the published version of the manuscript.

Acknowledgments

The authors would like to thank Dr. Idris Adanur for his contributions to the interpretation of the magnetic properties of MNPs. We would like to thank the Proofreading & Editing Office of the Dean for Research at Erciyes University for copyediting and proofreading service for this manuscript.

Conflicts of Interest

The authors declare no conflicts of interest.

Data Availability Statement

The data that support the findings of this study are available from the corresponding author upon reasonable request.

References

1. I. Jun, H.-S. Han, J. R. Edwards, and H. Jeon, “Electrospun Fibrous Scaffolds for Tissue Engineering: Viewpoints on Architecture and Fabrication,” *International Journal of Molecular Sciences* 19, no. 3 (2018): 745, <https://doi.org/10.3390/ijms19030745>.
2. B. Joseph, C. Jose, S. V. Kaval, et al., “Solvent-Casting Approach for Design of Polymer Scaffolds and Their Multifunctional Applications,” in *Functional Biomaterials: Design and Development for Biotechnology, Pharmacology, and Biomedicine*, eds. T. Mohan and K. S. Kleinschek (Weinheim, Germany: John Wiley & Sons, Ltd, 2023), 371–394.
3. A. Sola, J. Bertacchini, D. D’Avella, et al., “Development of Solvent-Casting Particulate Leaching (SCPL) polymer Scaffolds as Improved Three-Dimensional Supports to Mimic the Bone Marrow Niche,” *Materials Science and Engineering: C* 96 (2019): 153–165, <https://doi.org/10.1016/j.msec.2018.10.086>.
4. B. Aldemir Dikici and F. Claeysens, “Basic Principles of Emulsion Templating and Its Use as an Emerging Manufacturing Method of Tissue Engineering Scaffolds,” *Frontiers in Bioengineering and Biotechnology* 8 (2020): 554312, <https://doi.org/10.3389/fbioe.2020.00875>.
5. M. Costantini and A. Barbetta, “Gas Foaming Technologies for 3D Scaffold Engineering,” in *Functional 3D Tissue Engineering Scaffolds: Materials, Technologies, and Applications*, eds. Y. Deng and J. Kuiper (Amsterdam, The Netherlands: Elsevier, 2018), 127–149.
6. L. Ding, S. Song, L. Chen, et al., “A Freeze-Thawing Method Applied to the Fabrication of 3-d Curdlan/Polyvinyl Alcohol Hydrogels as Scaffolds for Cell Culture,” *International Journal of Biological Macromolecules* 174 (2021): 101–109, <https://doi.org/10.1016/j.ijbiomac.2021.01.160>.
7. A. Gleadall, D. Visscher, J. Yang, D. Thomas, and J. Segal, “Review of Additive Manufactured Tissue Engineering Scaffolds: Relationship Between Geometry and Performance,” *Burns & Trauma* 6 (2018): 19, <https://doi.org/10.1186/S41038-018-0121-4>.

8. A. Vaseashta, D. Demir, B. Sakım, M. Aşık, and N. Bölgen, "Hierarchical Integration of 3D Printing and Electrospinning of Nanofibers for Rapid Prototyping," in *Electrospun Nanofibers*, eds. A. Vaseashta and N. Bölgen (Cham, Switzerland: Springer, 2022), 631–655, https://doi.org/10.1007/978-3-030-99958-2_22.
9. S. Sa'adon, S. I. Abd Razak, A. E. Ismail, and K. Fakhruddin, "Fabrication of Dual Layer Polyvinyl Alcohol Transdermal Patch: Effect of Freezing-Thawing Cycles on Morphological and Swelling Ability," *Procedia Computer Science* 158 (2019): 51–57, <https://doi.org/10.1016/j.procs.2019.09.027>.
10. A. A. Adedoyin and A. K. Ekenseair, "Biomedical Applications of Magneto-Responsive Scaffolds," *Nano Research* 11 (2018): 5049–5064, <https://doi.org/10.1007/s12274-018-2198-2/metrics>.
11. L. F. Santos, A. S. Silva, and J. F. Mano, "Magnetic-Based Strategies for Regenerative Medicine and Tissue Engineering," *Advanced Healthcare Materials* 12 (2023): 2300605, <https://doi.org/10.1002/adhm.202300605>.
12. Y. Zhang, J. Li, and P. Habibovic, "Magnetically Responsive Nanofibrous Ceramic Scaffolds for On-Demand Motion and Drug Delivery," *Bioactive Materials* 15 (2022): 372–381, <https://doi.org/10.1016/j.bioactmat.2022.02.028>.
13. X. Hu, W. Liu, L. Sun, et al., "Magnetic Nanofibrous Scaffolds Accelerate the Regeneration of Muscle Tissue in Combination With Extra Magnetic Fields," *International Journal of Molecular Sciences* 23, no. 8 (2022): 4440, <https://doi.org/10.3390/ijms23084440>.
14. A. Dasari, J. Xue, and S. Deb, "Magnetic Nanoparticles in Bone Tissue Engineering," *Nanomaterials* 12 (2022): 757, <https://doi.org/10.3390/nano12050757>.
15. S. Leal-Marín, G. Gallaway, K. Höltje, A. Lopera-Sepulveda, B. Glasmacher, and O. Gryshkov, "Scaffolds With Magnetic Nanoparticles for Tissue Stimulation," *Current Directions in Biomedical Engineering* 7 (2021): 460–463, <https://doi.org/10.1515/cdbme-2021-2117>.
16. C. Shuai, W. Yang, C. He, et al., "A Magnetic Micro-Environment in Scaffolds for Stimulating Bone Regeneration," *Materials and Design* 185 (2020): 108275, <https://doi.org/10.1016/j.matdes.2019.108275>.
17. X. B. Zeng, H. Hu, L. Q. Xie, et al., "Magnetic Responsive Hydroxyapatite Composite Scaffolds Construction for Bone Defect Repair," *International Journal of Nanomedicine* 7 (2012): 3365–3378, <https://doi.org/10.2147/ijn.s32264>.
18. Y. Jia, M. Yuan, H. Yuan, et al., "Co-Encapsulation of Magnetic Fe₃O₄ Nanoparticles and Doxorubicin Into Biodegradable PLGA Nanocarriers for Intratumoral Drug Delivery," *International Journal of Nanomedicine* 7 (2012): 1697–1708, <https://doi.org/10.2147/ijn.s28629>.
19. J. Meng, B. Xiao, Y. Zhang, et al., "Super-Paramagnetic Responsive Nanofibrous Scaffolds Under Static Magnetic Field Enhance Osteogenesis for Bone Repair In Vivo," *Scientific Reports* 3 (2013): 1–7, <https://doi.org/10.1038/srep02655>.
20. D. Demir, D. Güreş, T. Tecim, R. Genç, and N. Bölgen, "Magnetic Nanoparticle-Loaded Electrospun Poly(ϵ -Caprolactone) Nanofibers for Drug Delivery Applications," *Applied Nanoscience* 8 (2018): 1461–1469, <https://doi.org/10.1007/S13204-018-0830-9>.
21. J. Zhang, S. Zhao, M. Zhu, et al., "3D-Printed Magnetic Fe₃O₄/MBG/PCL Composite Scaffolds With Multifunctionality of Bone Regeneration, Local Anticancer Drug Delivery and Hyperthermia," *Journal of Materials Chemistry B* 2 (2014): 7583–7595, <https://doi.org/10.1039/c4tb01063a>.
22. M. U. A. Khan, M. Rizwan, S. I. A. Razak, A. Hassan, T. Rasheed, and M. Bilal, "Electroactive Polymeric Nanocomposite BC-g-(Fe₃O₄/GO) Materials for Bone Tissue Engineering: In Vitro Evaluations," *Journal of Biomaterials Science. Polymer Edition* 33 (2022): 1349–1368, <https://doi.org/10.1080/09205063.2022.2054544>.
23. L. Garcíá, E. Garaio, A. López-Ortega, et al., "Fe₃O₄-SiO₂ Mesoporous Core/Shell Nanoparticles for Magnetic Field-Induced Ibuprofen-Controlled Release," *Langmuir* 39 (2023): 211–219, <https://doi.org/10.1021/acs.langmuir.2c02408>.
24. F. Ulusal, Z. Bilici, Y. Ozay, N. Özdemir, and N. Dizge, "Synthesis of Mesoporous Magnetic Fe₃O₄ Nanoparticles With Different Pore Sizes and Investigation of Dye Adsorption Capacities," *Particulate Science and Technology* 42 (2023): 804–814, <https://doi.org/10.1080/02726351.2023.2291770>.
25. F. Ulusal and N. Özdemir, "Synthesis and Characterization of Novel Mesoporous Fe₃O₄ Nanotubes for Drug Delivery," *Osmaniye Korkut Ata University. Journal of the Institute of Science and Technology* 6 (2023): 1353–1368.
26. S. Köse, "Investigation of the Mechanical and Physical Properties of Mesoporous Silicon Dioxide Fillet Epoxy Composites," *Journal of Radiation Research and Applied Science* 17 (2024): 100924, <https://doi.org/10.1016/j.jrras.2024.100924>.
27. F. Ayaz, D. Demir, and N. Bölgen, "Differential Anti-Inflammatory Properties of Chitosan-Based Cryogel Scaffolds Depending on Chitosan/Gelatin Ratio," *Artificial Cells, Nanomedicine, and Biotechnology* 49 (2021): 682–690, <https://doi.org/10.1080/21691401.2021.2012184>.
28. D. Demir, G. Goksen, S. Ceylan, M. Trif, and A. V. Rusu, "Optimized Peppermint Essential Oil Microcapsules Loaded Into Gelatin-Based Cryogels With Enhanced Antimicrobial Activity," *Polymers* 15, no. 13 (2023): 2782, <https://doi.org/10.3390/polym15132782>.
29. F. Öfkeli, D. Demir, and N. Bölgen, "Biomimetic Mineralization of Chitosan/Gelatin Cryogels and In Vivo Biocompatibility Assessments for Bone Tissue Engineering," *Journal of Applied Polymer Science* 138 (2021): 50337, <https://doi.org/10.1002/app.50337>.
30. Q. Ni, T. Zhu, W. Wang, et al., "Green Synthesis of Narrow-Size Silver Nanoparticles Using *Ginkgo biloba* Leaves: Condition Optimization, Characterization, and Antibacterial and Cytotoxic Activities," *International Journal of Molecular Sciences* 25, no. 3 (2024): 1913, <https://doi.org/10.3390/ijms25031913>.
31. Z. Zaheer, "Biogenic Synthesis, Optical, Catalytic, and In Vitro Antimicrobial Potential of ag-Nanoparticles Prepared Using Palm Date Fruit Extract," *Journal of Photochemistry and Photobiology B: Biology* 178 (2018): 584–592, <https://doi.org/10.1016/j.jphotobiol.2017.12.002>.
32. E. Łuczaj-Cepowicz, G. Marczuk-Kolada, A. Zalewska, M. Pawińska, and K. Leszczyńska, "Antibacterial Activity of Selected Glass Ionomer Cements," *Postępy Higieny i Medycyny Doświadczalnej* 68 (2014): 23–28, <https://doi.org/10.5604/17322693.1086069>.
33. K. El-Boubbou, R. Ali, H. Al-Zahrani, et al., "Preparation of Iron Oxide Mesoporous Magnetic Microparticles as Novel Multidrug Carriers for Synergistic Anticancer Therapy and Deep Tumor Penetration," *Scientific Reports* 9 (2019): 1–20, <https://doi.org/10.1038/s41598-019-46007-z>.
34. Y. Wei, B. Han, X. Hu, Y. Lin, X. Wang, and X. Deng, "Synthesis of Fe₃O₄ Nanoparticles and Their Magnetic Properties," *Procedia Engineering* 27 (2012): 632–637, <https://doi.org/10.1016/j.proeng.2011.12.498>.
35. S. Si, C. Li, X. Wang, D. Yu, Q. Peng, and Y. Li, "Magnetic monodisperse Fe₃O₄ nanoparticles," *Crystal Growth & Design* 5 (2005): 391–393, <https://doi.org/10.1021/CG0497905>.
36. K. Tao, H. Dou, and K. Sun, "Interfacial Coprecipitation to Prepare Magnetite Nanoparticles: Concentration and Temperature Dependence," *Colloids and Surfaces A: Physicochemical and Engineering Aspects* 320 (2008): 115–122, <https://doi.org/10.1016/j.colsurfa.2008.01.051>.
37. M. A. Ludeña, L. Meza F de, R. I. Huamán, et al., "Preparation and Characterization of Fe₃O₄/Poly(HEMA-Co-IA) Magnetic Hydrogels for Removal of Methylene Blue From Aqueous Solution," *Gels* 15, no. 10 (2023): 15, <https://doi.org/10.3390/gels10010015>.
38. X. Wang, S. Jing, Z. Hou, et al., "Permeable, Robust and Magnetic Hydrogel Beads: Water Droplet Templating Synthesis and Utilization

- for Heavy Metal Ions Removal,” *Journal of Materials Science* 53 (2018): 15009–15024, <https://doi.org/10.1007/S10853-018-2681-X>.
39. J. Zhi, Y. Wang, Y. Lu, J. Ma, and G. Luo, “In Situ Preparation of Magnetic Chitosan/Fe₃O₄ Composite Nanoparticles in Tiny Pools of Water-in-Oil Microemulsion,” *Reactive and Functional Polymers* 66 (2006): 1552–1558, <https://doi.org/10.1016/j.reactfunctpolym.2006.05.006>.
40. G. Ziegelberger, P. Vecchia, M. Hietanen, et al., “Guidelines on Limits of Exposure to Static Magnetic Fields,” *Health Physics* 96 (2009): 504–514, <https://doi.org/10.1097/01.hp.0000343164.27920.4a>.
41. H. Shao, J. Wu, S. Wang, et al., “3D gel-Printing of Porous Mg-Fe₂O₄ Magnetic Scaffolds for Bone Tissue Engineering,” *Ceramics International* 48 (2022): 7183–7191, <https://doi.org/10.1016/j.ceramint.2021.11.279>.
42. Z. Z. Zhang, D. Jiang, J. X. Ding, et al., “Role of Scaffold Mean Pore Size in Meniscus Regeneration,” *Acta Biomaterialia* 43 (2016): 314–326, <https://doi.org/10.1016/j.actbio.2016.07.050>.
43. C. M. Murphy and F. J. O’Brien, “Understanding the Effect of Mean Pore Size on Cell Activity in Collagen-Glycosaminoglycan Scaffolds,” *Cell Adhesion & Migration* 4 (2010): 377–381, <https://doi.org/10.4161/cam.4.3.11747>.
44. N. Abbasi, S. Hamlet, R. M. Love, and N. T. Nguyen, “Porous Scaffolds for Bone Regeneration,” *Journal of Science: Advanced Materials and Devices* 5 (2020): 1–9, <https://doi.org/10.1016/j.jsamd.2020.01.007>.
45. N. Annabi, J. W. Nichol, X. Zhong, et al., “Controlling the Porosity and Microarchitecture of Hydrogels for Tissue Engineering,” *Tissue Engineering. Part B, Reviews* 16 (2010): 371–383, <https://doi.org/10.1089/ten.teb.2009.0639>.
46. S. H. Moon, T. Y. Park, H. J. Cha, and Y. J. Yang, “Photo-/Thermo-Responsive Bioink for Improved Printability in Extrusion-Based Bioprinting,” *Materials Today* 25 (2024): 100973, <https://doi.org/10.1016/j.mtbio.2024.100973>.
47. F. F. Azhar, A. Olad, and R. Salehi, “Fabrication and Characterization of Chitosan-Gelatin/Nanohydroxyapatite-Polyaniline Composite With Potential Application in Tissue Engineering Scaffolds,” *Designed Monomers and Polymers* 17 (2014): 654–667, <https://doi.org/10.1080/15685551.2014.907621>.
48. J. Jafari, S. H. Emami, A. Samadikuchaksaraei, M. A. Bahar, and F. Gorjipour, “Electrospun Chitosan–Gelatin Nanofibrous Scaffold: Fabrication and In Vitro Evaluation,” *Bio-Medical Materials and Engineering* 21 (2011): 99–112, <https://doi.org/10.3233/bme-2011-06660>.
49. K. G. Dilruba Öznur and T. D. Ayşe Pınar, “Statistical Evaluation of Biocompatibility and Biodegradability of Chitosan/Gelatin Hydrogels for Wound-Dressing Applications,” *Polymer Bulletin* 81 (2024): 1563–1596, <https://doi.org/10.1007/S00289-023-04776-8>.
50. B. Ates, A. Ulu, S. Köytepe, S. A. Ali Noma, V. S. Kolat, and T. Izgi, “Magnetic-Propelled Fe₃O₄–Chitosan Carriers Enhance L-Asparaginase Catalytic Activity: A Promising Strategy for Enzyme Immobilization,” *Royal Society of Chemistry’s Advances* 8 (2018): 36063–36075, <https://doi.org/10.1039/c8ra06346j>.
51. L. Qiang, Z. Li, T. Zhao, S. Zhong, H. Wang, and X. Cui, “Atomic-Scale Interactions of the Interface Between Chitosan and Fe₃O₄,” *Colloids and Surfaces A: Physicochemical and Engineering Aspects* 419 (2013): 125–132, <https://doi.org/10.1016/j.colsurfa.2012.11.055>.
52. N. Malhotra, J. S. Lee, R. A. D. Liman, et al., “Potential Toxicity of Iron Oxide Magnetic Nanoparticles: A Review,” *Molecules* 25 (2020): 1–26, <https://doi.org/10.3390/molecules25143159>.
53. W. Yang, Y. Zhong, P. Feng, et al., “Disperse Magnetic Sources Constructed With Functionalized Fe₃O₄ Nanoparticles in Poly-L-Lactic Acid Scaffolds,” *Polymer Testing* 76 (2019): 33–42, <https://doi.org/10.1016/j.polymeresting.2019.03.008>.
54. W. Zhao, Z. Huang, L. Liu, W. Wang, J. Leng, and Y. Liu, “Porous Bone Tissue Scaffold Concept Based on Shape Memory PLA/Fe₃O₄,” *Composites Science and Technology* 203 (2021): 108563, <https://doi.org/10.1016/j.compscitech.2020.108563>.
55. X. Chen, X. Ge, Y. Qian, et al., “Electrospinning Multilayered Scaffolds Loaded With Melatonin and Fe₃O₄ Magnetic Nanoparticles for Peripheral Nerve Regeneration,” *Advanced Functional Materials* 30 (2020): 1–12, <https://doi.org/10.1002/adfm.202004537>.
56. R. de Santis, A. Gloria, T. Russo, et al., “A Route Toward the Development of 3D Magnetic Scaffolds With Tailored Mechanical and Morphological Properties for Hard Tissue Regeneration: Preliminary Study: A Basic Approach Toward the Design of 3D Rapid Prototyped Magnetic Scaffolds for Hard-Tissue Regeneration Is Presented and Validated in This Paper,” *Virtual and Physical Prototyping* 6 (2011): 189–195, <https://doi.org/10.1080/17452759.2011.631324>.
57. J. Ge, R. Asmatulu, B. Zhu, Q. Zhang, and S. Y. Yang, “Synthesis and Properties of Magnetic Fe₃O₄/PCL Porous Biocomposite Scaffolds With Different Sizes and Quantities of Fe₃O₄ Particles,” *Bioengineering* 9, no. 7 (2022): 278, <https://doi.org/10.3390/bioengineering9070278>.
58. R. Sun, H. Chen, J. Zheng, et al., “Composite Scaffolds of Gelatin and Fe₃O₄ Nanoparticles for Magnetic Hyperthermia-Based Breast Cancer Treatment and Adipose Tissue Regeneration,” *Advanced Healthcare Materials* 12 (2023): 1–13, <https://doi.org/10.1002/adhm.202202604>.
59. S. Panseri, A. Russo, G. Giavaresi, et al., “Innovative Magnetic Scaffolds for Orthopedic Tissue Engineering,” *Journal of Biomedical Materials Research Part A* 100 (2012): 2278–2286.
60. A. Guarnieri, M. Triunfo, C. Scieuzo, et al., “Antimicrobial Properties of Chitosan From Different Developmental Stages of the Bioconverter Insect *Hermetia illucens*,” *Science Reports* 121, no. 12 (2022): 1–12, <https://doi.org/10.1038/s41598-022-12150-3>.
61. D. Yan, Y. Li, Y. Liu, N. Li, X. Zhang, and C. Yan, “Antimicrobial Properties of Chitosan and Chitosan Derivatives in the Treatment of Enteric Infections,” *Molecules* 26, no. 23 (2021): 7136, <https://doi.org/10.3390/molecules26237136>.
62. J. Sougata and J. Subrata, eds., *Functional Chitosan: Drug Delivery and Biomedical Applications* (Singapore: Springer Nature, 2019), 457–489.